

Quantum caustics in resonance fluorescence trajectories

M. Naghiloo,¹ D. Tan,¹ P. M. Harrington,¹ P. Lewalle,² A. N. Jordan,^{2,3,4} and K. W. Murch^{1,5}

¹*Department of Physics, Washington University, St. Louis, Missouri 63130*

²*Department of Physics and Astronomy, University of Rochester, Rochester, NY 14627*

³*Center for Coherence and Quantum Optics, University of Rochester, Rochester, NY 14627*

⁴*Institute for Quantum Studies, Chapman University, Orange, CA 92866*

⁵*Institute for Materials Science and Engineering, St. Louis, Missouri 63130*

We employ phase-sensitive amplification to perform homodyne detection of the resonance fluorescence from a driven superconducting artificial atom. Entanglement between the emitter and its fluorescence allows us to track the individual quantum state trajectories of the emitter conditioned on the outcomes of the field measurements. We analyze the ensemble properties of these trajectories by considering trajectories that connect specific initial and final states. By applying the stochastic path integral formalism, we calculate equations-of-motion for the most likely path between two quantum states and compare these predicted paths to experimental data. Drawing on the mathematical similarity between the action formalism of the most likely quantum paths and ray optics we study the emergence of caustics in quantum trajectories—places where multiple extrema in the stochastic action occur. We observe such multiple most likely paths in experimental data and find these paths to be in reasonable quantitative agreement with theoretical calculations.

I. INTRODUCTION

In ray optics, light travels the shortest optical path between two points. While this minimizes the action associated with the path, multiple minima in the action may occur under some circumstances. These phenomena, known as caustics, are described by catastrophe theory [1, 2], which deals with discontinuous and divergent phenomena and is applicable to topics ranging from biology to social science [3]. Caustics are well-studied in optics and have been extended to stochastic media for which the conditions are described by fixed statistical models [1, 4]. In analogy to the trajectory of light propagating in a turbulent medium, a continuously-monitored quantum system also undergoes stochastic trajectories in its quantum state space due to the back-action of continuous measurement [5–7]. Similarly for rays in optics, stochastic path integral formalism has been applied to the dynamics of diffusive quantum trajectories, revealing optimal quantum paths connecting two points in quantum state space [8–10].

The probability density associated with a particular quantum trajectory may be described with a stochastic action; just as an action may be optimized to obtain classical paths in Lagrangian or Hamiltonian mechanics, the stochastic action in a path integral may be extremized to obtain optimal paths through the state space of a measured quantum system. Such most-likely paths (MLPs) have been studied in the context of continuous quantum non-demolition and fluorescence measurements [8, 9, 11], quantum entanglement [12], and the stochastic path integral formalism has been applied to calculate correlation functions in measurement observables [10]. More broadly, MLPs have been applied to general diffusion processes [13] and the case of chemical kinetics where multiple MLPs have been predicted for classical stochastic dynamics [14, 15].

Here we report on the observation of individual quan-

tum trajectories via homodyne monitoring of resonance fluorescence from a superconducting qubit. By analyzing trajectories meeting the same pre- and post-selection, we identify optimal quantum paths which are in agreement with the paths predicted from the path integral formalism. As with optical caustics, the path integral formalism predicts the existence of multiple optimal paths for quantum trajectories [16]. Under driving conditions where such *quantum caustics* are predicted to occur, we find that our observed quantum trajectories naturally split into two communities [17–19]. We show number of captured trajectories in each community and associated MLPs are in quantitative agreement with the theory prediction. Our results provide insight into the fundamental light matter interaction of resonance fluorescence and highlight the connection between quantum dynamics and divergent systems, offering routes to investigate the possibility of chaos and understand the quantum classical boundary.

II. QUANTUM TRAJECTORIES IN RESONANCE FLUORESCENCE

Our experiment focuses on the stochastic trajectories of a driven quantum emitter that interacts radiatively with its environment. The combination of resonant drive and decay—resonance fluorescence—results in emitted light with uniquely quantum features that have been studied extensively in atomic and condensed matter systems [20–27]. In departure from conventional studies of resonance fluorescence, here we approach the quantum dynamics of resonance fluorescence in the context of quantum measurement and use the fluorescence signal to calculate quantum trajectories for the emitter’s state. The experiment consists of an effective two-level system (qubit) resulting from the resonant interaction between a transmon circuit [28] and a 3D aluminum cavity [29].

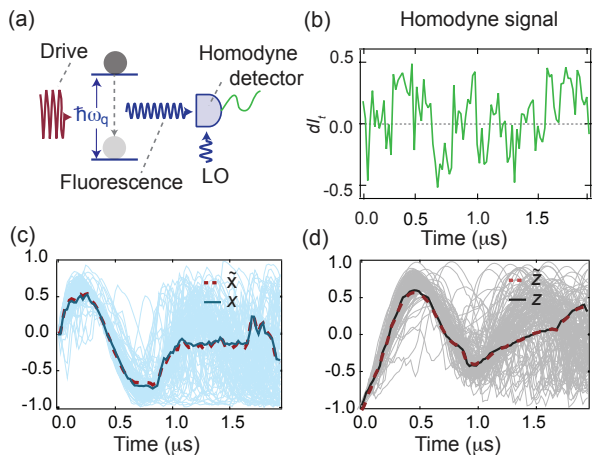


Figure 1: **Resonance fluorescence quantum trajectories.**

(a), The experiment uses a near-quantum limited Josephson parametric amplifier to perform homodyne measurement of the fluorescence emitted by an effective two-level system which is realized by resonant interaction of a transmon circuit and a 3D aluminum cavity. (b), The dimensionless homodyne signal (denoted dI_t at time step t) reflects the quantum fluctuations of the measured electromagnetic mode and is normalized so that its variance is γdt . (c,d), The x and z components of several trajectories calculated using the SME and homodyne signal. A specific trajectory (\tilde{x}, \tilde{z}) is compared to its tomographic reconstruction (x, z). The close agreement between the curves indicates that the SME faithfully tracks the quantum state.

The qubit decay is set by deliberate coupling of the cavity to a 50Ω microwave transmission line allowing the fluorescence signal to be collected with high efficiency (Fig. 1a). The effective Hamiltonian of the system under the rotating wave approximation is ($\hbar = 1$),

$$H = -\frac{\omega_q}{2}\sigma_z - \frac{\Omega}{2}\sigma_y + \gamma(a^\dagger\sigma_- + a\sigma_+), \quad (1)$$

where the three terms in the Hamiltonian describe the qubit, the drive, and the resonant interaction of qubit and environment, respectively. Here, $a(a^\dagger)$ is annihilation(creation) operator for the quantized field in the transmission line and the qubit is a pseudo-spin system described by the Pauli spin operators $\sigma_x, \sigma_y, \sigma_z$ and σ_\pm .

We use a near-quantum-limited Josephson parametric amplifier to perform phase sensitive amplification of a single field quadrature $\propto (a^\dagger e^{i\phi} + a e^{-i\phi})$ of the fluorescence. By virtue of the interaction Hamiltonian, this quadrature of the field is correlated with a specific dipole of the emitter, $\sigma_- e^{i\phi} + \sigma_+ e^{-i\phi}$. Measurements of this quadrature amplitude therefore convey information about the emitter and can be used to reconstruct the evolution of the emitter's state [30]. Under appropriate scaling, the digitized measurement signal is represented by (for $\phi = 0$),

$$dI_t = \sqrt{\eta}\gamma\langle\sigma_x\rangle dt + \sqrt{\gamma}\xi_t dt. \quad (2)$$

The measurement signal is proportional to $\langle\sigma_x\rangle$, but also

contains a zero-mean random increment, ξ_t , with variance of dt^{-1} , arising from the quantum fluctuations of the field. Here, $\eta = 0.45$ is the quantum efficiency and $\gamma = 1.42 \mu\text{s}^{-1}$ is the decay rate of the emitter which characterizes the measurement strength [30]. The random increments ξ_t imply a stochastic evolution for the emitter's state, represented by density matrix ρ , which can be calculated by the corresponding stochastic master equation (SME) [31],

$$\dot{\rho} = -i\frac{\Omega}{2}[\sigma_y, \rho] + \gamma\mathcal{D}[\sigma_-]\rho + \sqrt{\gamma\eta}\mathcal{H}[\sigma_-]\rho\xi_t, \quad (3)$$

where $\mathcal{D}[\sigma_-]$ and $\mathcal{H}[\sigma_-]$ are the dissipation and jump superoperators respectively [31]. We may recast this stochastic master equation in Bloch vector components, $x \equiv \langle\sigma_x\rangle$ and $z \equiv \langle\sigma_z\rangle$, as follows,

$$\begin{aligned} \dot{z} &= +\Omega x + \gamma(1-z) + \sqrt{\eta\gamma}x(1-z)\xi_t, \\ \dot{x} &= -\Omega z - \frac{\gamma}{2}x + \sqrt{\eta}(1-z-x^2)\xi_t, \end{aligned} \quad (4)$$

where the initial state, homodyne measurement phase, and drive Hamiltonian (characterized by a Rabi frequency $\Omega/2\pi = 0.9$ MHz) allow us to restrict the evolution to the x - z plane of the Bloch sphere.

Figure 1 depicts the quantum trajectories that are calculated for the emitter as it evolves due to both unitary drive and radiative decay. The quantum trajectories exhibit stochastic features associated with the back-action of homodyne measurement of the fluorescence [30] and evolution originating from the unitary drive. The calculated quantum trajectories are validated with quantum state tomography to verify the predicted expectation values $\langle\sigma_x\rangle, \langle\sigma_z\rangle$ are in agreement with the average outcomes of projective measurements. Figure 1c,d show the close agreement between a specific trajectory and reconstructed trajectory by the state tomography technique described in previous work [7, 9, 30].

III. MOST LIKELY QUANTUM PATH

We return to the analogy between the stochastic trajectories of the emitter's state in quantum phase space and stochastic trajectories in optics such as starlight twinkling through a turbulent atmosphere. In both cases the randomness immediately suggests the question of statistical character. What is the most probable path for the system for a given initial and final state? To address this question we examine the relation between the homodyne signal and the state coordinate x (Eq. 2). As shown in Fig. 2, the detected signal is Gaussian distributed about x ; signals with values in a region close to $\sqrt{\eta}\gamma x dt$ are more probable than signals in that vary significantly from this mean value. In a given trajectory, the measurement results lead to stochastic evolution of the state coordinates (x, z) , but the distribution of measurement results follows the evolution of x ; the detection signals and state

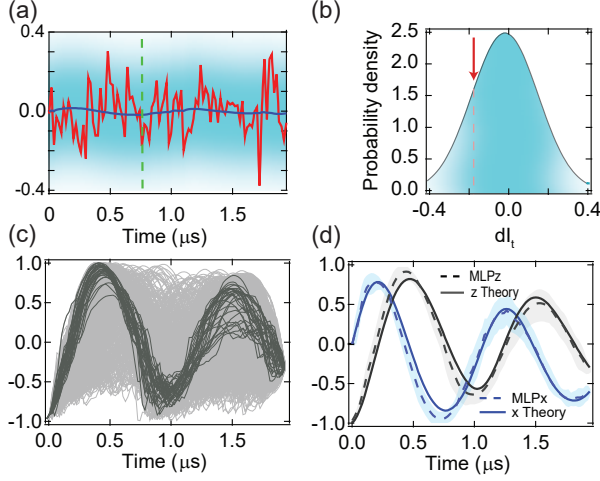


Figure 2: **Path probability and most likely paths.** (a), Demonstration of path-probability calculation. The blue curve indicates $\sqrt{\eta\gamma}x dt$ which determines the probability distribution (blue background color) for a corresponding homodyne signal (red curve). (b), A cross-section of the probability density at the time indicated by the dashed green line of (a). The Gaussian distribution is shifted from zero by $\sqrt{\eta\gamma}x dt$. The arrow shows the value of homodyne signal at that point. (c), The pre- and post-selected trajectories for initial $\{z(0), x(0)\} = \{-0.97, 0\}$ and final $\{z(1.94 \mu\text{s}), x(1.94 \mu\text{s})\} = \{-0.3, -0.6\}$ boundary condition (only z traces are shown). The top five percent of which have lowest Euclidean distance from others are highlighted in black. (d), Solid black(blue) line is the theoretical MLP for $z(x)$ obtained from Eqs. (6). The dashed lines are the corresponding experimental MLP obtained by averaging the highlighted trajectories. The shaded area along experimental curves shows the standard deviation of the averaged trajectories.

trajectories are thus coupled, leading to rich phenomena associated with state and signal correlations [11, 32–34].

Considering this state-signal correlation, we are able to calculate the joint probability density for each measurement signal (dI_t) and state coordinates $\mathbf{q} \equiv (x, z)$ with initial state \mathbf{q}_0 and final state \mathbf{q}_N ,

$$P_{\text{joint}} = \delta^{(2)}(\mathbf{q} - \mathbf{q}_0)\delta^{(2)}(\mathbf{q} - \mathbf{q}_N) \prod_{n=0}^{N-1} \mathcal{P}_n(dI_t|\mathbf{q}). \quad (5)$$

Where $\mathcal{P}_n(dI_t|\mathbf{q})$ is the probability density for signal dI_t at time $t = n dt$ and N is the total number of time steps. The most likely path maximizes the total path probability density P_{joint} . To find this path we introduce a stochastic path integral representation of the joint probability, $P_{\text{joint}} \propto \int \mathcal{D}\mathbf{p} e^{\mathcal{S}}$. The term \mathcal{S} is the stochastic action and $\mathcal{D}\mathbf{p}$ is an integral measure over the conjugate variables (p_x, p_z) which are auxiliary dynamical parameters that impose the correct quantum measurement back-action dynamics [8, 10]. This approach has been verified experimentally for continuous quantum non-demolition measurement [9]. Here we adopt the path integral formalism for homodyne detection of resonance fluorescence to obtain a corresponding stochastic Hamiltonian whose solutions (via Hamilton's equations) are the most-likely paths (MLPs). This is related to the stochastic ac-

tion, $\mathcal{S} = \int [-\dot{\mathbf{q}} \cdot \mathbf{p} + \mathcal{H}] dt$, as discussed at length in [8, 10, 11, 16]. The full stochastic Hamiltonian for our driven-fluorescence system, using all three dimensions $x \in [-1, 1]$, $y \in [-1, 1]$ and $u \in [0, 2]$ ($u = 1 + z$, for compactness) of the Bloch sphere, may be derived using the master equation (Eq. 3) and methods described in Ref. [11], which yield

$$\begin{aligned} \mathcal{H} = & p_u \left[\Omega x + u\gamma \left(1 - 2\eta + \frac{\eta u}{2} \right) \right. \\ & \left. + \sqrt{\eta\gamma}xr(2 - u) + 2\gamma(\eta - 1) \right] \\ & + p_x \left[-\Omega(1 - u) - \frac{\gamma}{2}x(1 + \eta u - 2\eta) \right. \\ & \left. + \sqrt{\eta\gamma}(2 - u - x^2)r \right] \\ & + p_y \left[-\frac{\gamma}{2}y(1 + \eta u - 2\eta) - \sqrt{\eta\gamma}xyr \right] \\ & - \frac{r^2}{2} + r\sqrt{\eta\gamma}x - \frac{\eta\gamma u}{2}. \end{aligned} \quad (6)$$

The stochastic readout is given by r , γ is the fluorescence rate, η the measurement efficiency, and Ω denotes the Rabi frequency.

For our case, where the dynamics is restricted to the x - z plane of the Bloch sphere, we may eliminate \dot{y} and \dot{p}_y by setting $y = 0$ (setting $y = 0$ decouples p_y from the remaining equations regardless of its value). This simplification leads to a reduced stochastic Hamiltonian inhabiting a four, rather than six-dimensional phase space:

$$\begin{aligned} H = & p_u \left[\Omega x + u\gamma \left(1 - 2\eta + \frac{\eta u}{2} \right) \right. \\ & \left. + \sqrt{\eta\gamma}xr(2 - u) + 2\gamma(\eta - 1) \right] \\ & + p_x \left[-\Omega(1 - u) - \frac{\gamma}{2}x(1 + \eta u - 2\eta) \right. \\ & \left. + \sqrt{\eta\gamma}(2 - u - x^2)r \right] \\ & - \frac{r^2}{2} + r\sqrt{\eta\gamma}x - \frac{\eta\gamma u}{2}. \end{aligned} \quad (7)$$

Since H is time-independent, each MLP conserves a “stochastic energy” $E = H$. The deterministic equations-of-motion are

$$\dot{z} = +\Omega x + \gamma(1 - z) \left(1 - \frac{\eta(1 - z)}{2} \right) + \sqrt{\eta\gamma}x(1 - z)r, \quad (8a)$$

$$\dot{x} = -\Omega z - \frac{\gamma}{2}x(1 - \eta(1 - z)) + \sqrt{\eta\gamma}(1 - z - x^2)r, \quad (8b)$$

$$\begin{aligned} \dot{p}_z = & -\gamma p_z(1 - \eta(1 - z) + \sqrt{\eta\gamma}xr) \\ & + p_x(\Omega + \gamma\eta x/2 + \sqrt{\eta\gamma}r) - \eta\gamma/2, \end{aligned} \quad (8c)$$

$$\begin{aligned} \dot{p}_x = & -p_z(\Omega + \sqrt{\eta\gamma}(1 - z)r) + p_x(\gamma(1 - \eta(1 - z))/2 \\ & + 2\sqrt{\eta\gamma}xr) - \sqrt{\eta\gamma}r, \end{aligned} \quad (8d)$$

where $r = \sqrt{\eta\gamma}[x + p_x(1 - z - x^2) + p_zx(1 - z)]$ is the (deterministic) optimal signal that replaces the ho-

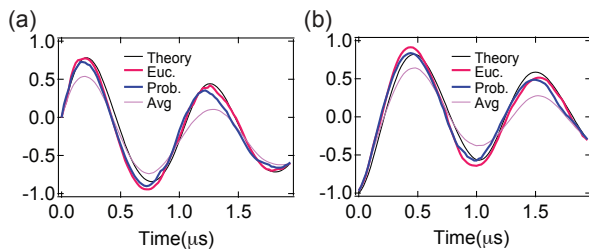


Figure 3: **Comparison of different experimental measures for most likely paths.** We compare the two different measures for experimental MLPs to theory for for initial $\{z(0), x(0)\} = \{-0.97, 0\}$ and final $\{z(1.94 \mu\text{s}), x(1.94 \mu\text{s})\} = \{-0.3, -0.6\}$ states (panels (a,b) show trajectories for x, z respectively). The Euclidean distance method (red) and path probability density maximization (blue) are both in close agreement with theory (black). The average of the full ensemble of pre- and post-selected trajectories (gray) deviates significantly from the MLP.

modyne signal (Eq. 2) dI/dt . The first two equations are comparable with the SME we use to update the experimental quantum trajectories (in Stratonovich form), and the last two equations pertain to the auxiliary parameters. The four equations-of-motion for the most likely path involving z, x, p_z, p_x in Eqs. (8), combined with the constraint for r , may be solved numerically given initial and final states as we show in Fig. 2d (solid curves) for initial $\{z(0), x(0)\} = \{-0.97, 0\}$ and final $\{z(1.94 \mu\text{s}), x(1.94 \mu\text{s})\} = \{-0.3, -0.6\}$. Analytical solutions for these equations-of-motion for unity quantum efficiency and pure state evolution are discussed in Appendix VI.

We now turn to the experimental investigation of the most likely path. To experimentally determine the most likely path we examine the Euclidean distance $d_i \equiv \frac{1}{M-1} \sum_{j \neq i}^M \sum_{k=0}^{N-1} ((x_{i,k} - x_{j,k})^2 + (z_{i,k} - z_{j,k})^2)$ between each trajectory and all other trajectories in the ensemble. Because the MLP should capture the highest density of other trajectories in a nearby vicinity, trajectories that minimize the Euclidean distance to others in the set should closely approximate the MLP. As such, we rank the trajectories in order of increasing d_i and average the top few percent. This method was used to compare experiment and theory in the case of continuous quantum non-demolition measurement [9]. From an ensemble of $\sim 10^5$ trajectories initialized in the excited state ($z = -0.97$), we post-select a sub-ensemble of trajectories that achieve a final given boundary condition, $\{z, x\} = \{-0.3, -0.6\}$ at $t = 1.94 \mu\text{s}$, within a selection tolerance of ± 0.05 as shown for z in Fig. 2c. These trajectories are ranked according to the minimum Euclidean distance from all other trajectories and of these we highlight the closest 5%. As shown in Fig. 2d, the average of these selected trajectories is in good agreement with the theoretical MLP.

An alternate method to determine MLP is to simply calculate the total path probability density (via Eq. 5)

and average the top 5% of trajectories with the highest path probability density. This naturally approximates the MLP. In Fig. 3 we compare these two methods and find that both methods to produce experimental MLPs that are in close agreement with theory. In contrast, a simple average of all of the pre- and post-selected trajectories is in clear disagreement with the theoretical MLP.

IV. MULTIPLE MOST LIKELY PATHS

The MLP is the solution for the equations-of-motion, Eqs. (8). Now, it is natural to ask if these equations-of-motion have more than one solution as suggested from the presence of caustics in ray optics. Multiple solutions exist at states where a Lagrangian manifold in MLP phase space overlaps itself, either through a fold or divergence of the manifold [35, 36], or at a “winding number” overlap caused by the manifold wrapping over itself as constituent paths orbit the Bloch sphere at different speeds [16]. In either case, we expect distinct clusters of stochastic trajectories corresponding to the different MLPs. As shown in Fig. 4, we may find such solutions theoretically, in Eqs. (8), by choosing an initial state coordinate \mathbf{q}_i , and sweeping through different initial momenta \mathbf{p}_i ; this defines the Lagrangian manifold we use throughout the subsequent analysis. Evolution under Eqs. (8) deforms this initially flat, vertical plane in MLP phase space because different initial momenta result in different final states. When the manifold is no longer a one-to-one function between \mathbf{q} and \mathbf{p} , multiple paths corresponding to extrema in the stochastic action connect the initial and final states.

We note that in the absence of drive, the evolution of the qubit is constrained to a deterministic ellipse for a given evolution time [30, 37, 38]. In this case, the Lagrange Manifold is constrained to these deterministic ellipses. As a result the manifold is always a one-to-one function between \mathbf{q} and \mathbf{p} , and multiple-MLPs are not possible. As seen in Fig. 4b,c the drive breaks this one-to-one character leading to an increasing number of MLPs for longer evolution times.

In order to confirm the presence of these multiple-MLPs in experimental data, we pre- and post-select the trajectories by the given boundary conditions. While the experimental trajectories do not exactly follow one or the other MLP, the MLP solutions should approximate the paths taken by many of the individual trajectories. In this case, the pre- and post-selected trajectories should belong to two different groups, such that the mean Euclidean distance between the members in each group is minimized. Therefore, we need a clustering algorithm [17–19] that efficiently separates these trajectories into two groups. In order to perform clustering, for each N -step trajectory we define the weighted mean Euclidean distance to other elements of the set $d_i^W \equiv \frac{1}{M-1} \sum_{j \neq i}^M \sum_{k=0}^{N-1} P_j ((x_{i,k} - x_{j,k})^2 + (z_{i,k} - z_{j,k})^2)$ and define the average weighted Euclidean distance of the set

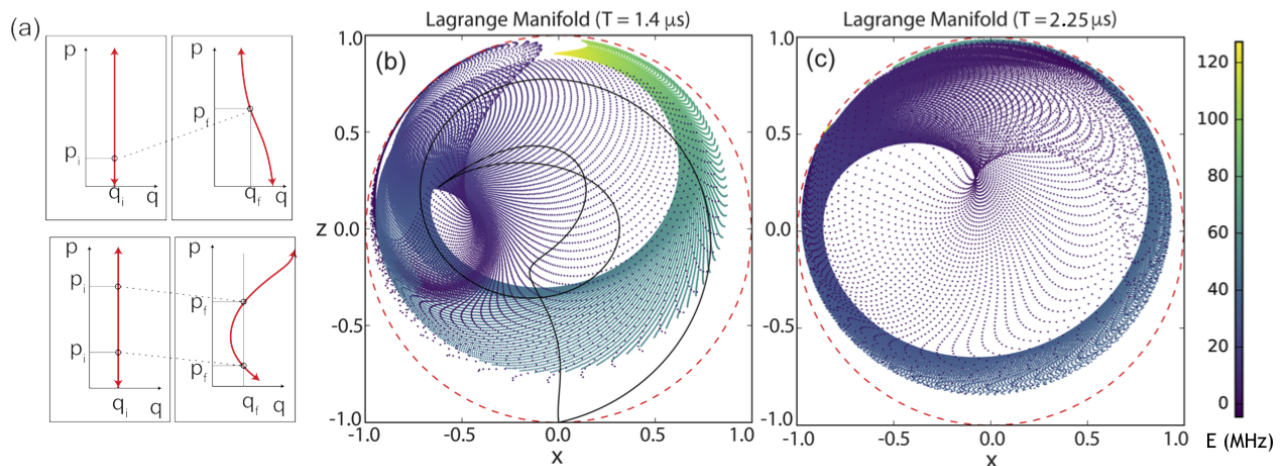


Figure 4: **The Lagrange Manifold.** (a), Schematic representation of Lagrange manifold folding leading to multiple most likely paths. For an initial state $\{z_i, x_i\}$ we consider all possible initial momenta, represented as a vertical red line. Evolution under Eqs. (8) results in different final states for different initial momenta specifying the most likely path that connects initial and final states, as shown in the left panels. When the red curve fails the vertical line test as shown in the right panels, multiple initial momenta result in the same final state. (b,c), The Lagrange manifold used to find MMLPs in this system is a two-dimensional object in a four-dimensional Hamiltonian phase space; we show its projection into the x - z plane of the Bloch sphere. A sampled range of momenta $\{p_{zi}, p_{xi}\}$ are initialized for the state $(\{z_i, x_i\} = \{-1, 0\})$ at $t = 0$ and allowed to evolve up to $T = 1.4 \mu s$ (b) and $T = 2.25 \mu s$ (c); each point in the scatter plot corresponds to a path generated by a different initial momentum. Compare with panel (a); just as a line of all p may intersect the manifold one or more times at a given q_f , we may now imagine sticking a pin into the figure at a particular point $\{z_f, x_f\}$, which might go through one or more layers of the manifold. Each intersection or layer corresponds to a distinct path reaching the chosen final state. Caustic regions emanating from a catastrophe in the manifold are clearly visible at both of the times shown above. The counter-clockwise spiraling of the manifold is the result of the Rabi drive applied to the qubit; we see that overlap in the manifold due to this spiraling matures into a cusp catastrophe over time. Color denotes stochastic energy E for each path. The two theory MLPs which are compared with data in Fig. 5 are shown superposed in black in panel (b); these are the paths which two distinct points on the manifold trace out as it evolves and folds over itself.

as $\bar{d}^W = \frac{1}{M} \sum_{i=1}^M d_i^W$, where M is the number of trajectories in the set and P_j is a weighting factor that is proportional to the logarithm of the probability for trajectory j as determined from Eq. 5. The algorithm aims to separate the ensemble into two clusters that minimize the sum of the weighted Euclidean distance between members of each set, $\bar{d}_{\text{set1}}^W + \bar{d}_{\text{set2}}^W$. The clustering algorithm starts by randomly splitting the ensemble of trajectories into two sets. In each iteration of the algorithm the weighted distance, d_i^W , given a randomly chosen trajectory i , is calculated for each set and the trajectory i is added to the set that minimizes $\bar{d}_{\text{set1}}^W + \bar{d}_{\text{set2}}^W$. The algorithm proceeds through the ensemble of trajectories by transferring trajectories between clusters to minimize the average weighted distance. We find that the algorithm typically finds the optimal configuration in $\simeq M$ steps and finds the same clustering configuration independent of the initial random configuration (see Figure 5a,b). The weighting factor P_j helps the algorithm converge to the final configuration faster, but does not substantially affect the final cluster distributions.

By averaging the individual paths of each group that have the minimum Euclidean distance from other members in each set, we obtain the experimental most likely paths (5c,d). These experimental MLPs are in reasonable agreement with the two MLPs terminating at the desired boundary conditions.

While the occurrence of multiple most likely paths is

associated with multiple extrema of the stochastic action, these solutions may have different values of stochastic action—meaning that the paths have different total path probability densities. We can check if these path probability densities are accurately represented by the relative occurrence of paths in each cluster.

Figure 6a displays a histogram of the Euclidean distance, \mathcal{E} , of trajectories from their MLP in each set. Given the fact that the MLP captures most trajectories in its vicinity, one would think these histograms would acquire a maximum at $\mathcal{E} = 0$ and decrease as we go far from the MLP. However, the multiplicity increases for trajectories with larger \mathcal{E} and the peak of the histogram occurs for non-zero \mathcal{E} . The multiplicity, $n(\mathcal{E})$ which accounts for the number of different trajectories that have same Euclidean distance \mathcal{E} from a MLP is given by the number of ways a Euclidean distance can be obtained from N timesteps, $\mathcal{E}_1^2 + \mathcal{E}_2^2 + \dots + \mathcal{E}_N^2 = \mathcal{E}^2$, where \mathcal{E}_i is the deviation from the MLP at the i^{th} time step.

With this understanding of the multiplicity, the distribution of trajectories attaining an average Euclidean distance from the MLP, $H(\mathcal{E})$, is given by the product of the path probability distribution and the multiplicity $H(\mathcal{E}) = P(\mathcal{E}) \times n(\mathcal{E})$,

$$H(\mathcal{E}) = P(0)e^{-\frac{\mathcal{E}^2}{2\sigma^2}} \times \frac{2\pi^{N/2}}{\Gamma(\frac{N}{2})} \mathcal{E}^{N-1}, \quad (9)$$

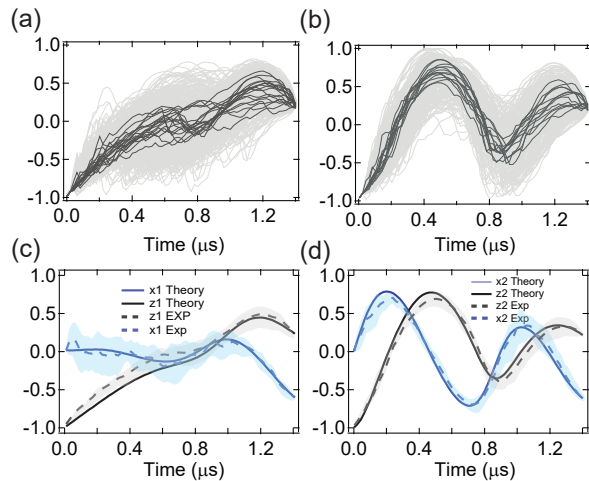


Figure 5: **Experimental multiple most likely paths.** (a,b), By applying a clustering algorithm to experimental trajectories that attain the chosen initial and final boundary conditions we obtain two groups that minimize the mean Euclidean distance between members of each group. The trajectories in each group with lowest Euclidean distance from other members in the group are highlighted in black (z trajectories are shown). (c,d), Comparison to theory; the solid curves are theory predictions and the dashed lines are obtained from averaging the highlighted experimental trajectories. The shaded area along experimental curves shows the standard deviation of the averaged trajectories.

where we assume that $P(\mathcal{E})$ is a half-normal distribution centered at zero and characterized by the variance σ^2 . The multiplicity $n(\mathcal{E})$ is given by the area of an N -dimensional hypersphere, and Γ is the Gamma function. The variance σ^2 can be determined directly, given the fact that $H(E)$ acquires its maximum at $\mathcal{E} = \sigma\sqrt{N-1}$. Since we are interested in the relative probability of two MLPs, $P_1(0)/P_2(0)$ we divide two experimental histograms,

$$\frac{H_1(\mathcal{E})}{H_2(\mathcal{E})} = \frac{P_1(0)}{P_2(0)} \exp \left[-\frac{\mathcal{E}^2}{2} \left(\frac{1}{\sigma_1^2} - \frac{1}{\sigma_2^2} \right) \right], \quad (10)$$

and fit this function to the data to extract the relative probability. We show the result in Fig. 6 which has reasonable agreement with the theoretical path probability values calculated by stochastic action.

Looking at the two MLPs shown in Figs. 4 and 5, we immediately see that they have different winding numbers about the Bloch sphere (see the appendices, and/or Ref. [16] for a discussion of winding number MMLPs). A given noise realization or measurement record can move the state approximately with the Rabi drive, or move the state substantially ahead or behind the drive; thus it is possible to obtain MLPs which end at the same state, having gone around the Bloch sphere a different number of times. What we have with the MMLP example shown is (1) a path which moves approximately with the drive, and (2) a path whose initial momentum corresponds to an optimal readout which lags behind the drive, such that it reaches the given final state with one less winding count. In summary, quantum dynamics of the MLP is

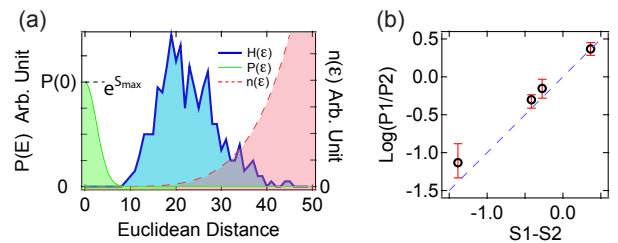


Figure 6: **Relative probability of multiple most likely paths.** (a), The peak of the probability density distribution of the Euclidean distance from the MLP (green) is related to the extremum of the stochastic action (\mathcal{S}_{\max}). The observed distribution (blue) has a maximum that shifted from 0 due to the increasing multiplicity of trajectories with a larger Euclidean distance from the MLP. (b), To compare the experimental distributions to the theoretical stochastic entropy maxima, we use the multiplicity ($n(\mathcal{E})$) and observed distribution $H(\mathcal{E})$ to determine $P(0)$. We compare the relative probability ($P(0)_{\text{cluster1}}/P(0)_{\text{cluster2}}$) to the predicted relative probability $S_1 - S_2$. Error bars indicate the uncertainty in the fit to the relative distribution. We apply this analysis to 4 different MMLP pairs with initial state $\{z(0), x(0)\} = \{-0.97, 0\}$ and final states $\{z(T), x(T), T(\mu\text{s})\} = \{0.65, -0.08, 1.2\}$, $\{0.19, -0.93, 1.4\}$, $\{0.36, 0.47, 1\}$, $\{0.21, -0.62, 1.4\}$, (left to right on graph).

given by the competition between the stochastic evolution associated with measurement and the unitary evolution arising from the drive. Different MLPs occur when one or the other types of evolution dominate at different times. This example illustrates that the existence of several MLPs arises from the presence of several different effects in the system; they can each take precedence over the other, in a given case, and generate qualitatively different behaviors that land at the same final state.

V. CONCLUSION

In the absence of measurement, a closed quantum system has a dynamics that is described by the Schrödinger equation. Given the initial condition, a *unique, deterministic* solution emerges that specifies the quantum state at all future times. In contrast, resonance fluorescence is an intrinsically open quantum system phenomenon, leading to a dynamics that differs dramatically from that of a closed system. This difference is highlighted in the phenomenon of *quantum caustics*; even for relatively short periods of evolution, catastrophes may form in manifolds of the most-likely path phase space, generating caustic regions where several most-likely paths link a given initial and final state over a given time evolution. By understanding multiple most likely paths through this catastrophe formation in the manifold, we see an analogy between the multiple-path propagation of our quantum trajectories, and caustic phenomena in optical propagation through random media. These phenomena may have important consequences for quantum control, and

opens new possibilities in the investigation of dynamical instabilities and chaos in continuously measured quantum systems.

Acknowledgment

We acknowledge helpful discussions and early contributions from A. Chantasri. We acknowledge primary research support from the John Templeton Foundation grant ID 58558, NSF grants DMR-1506081 and PHY-1607156, and secondary support for personnel from the ONR No. 12114811 and the ARO No. W911NF-15-1-0496. This research used facilities at the Institute of Materials Science and Engineering at Washington University. K.W.M acknowledges support from the Sloan Foundation.

VI. APPENDIX: REDUCTION OF THE STOCHASTIC HAMILTONIAN

We may reduce our stochastic Hamiltonian Equ. 7 to an even simpler form. Consider a canonical transformation from Cartesian to polar coordinates,

$$\begin{pmatrix} x \\ z \\ p_x \\ p_z \end{pmatrix} = \begin{pmatrix} R \sin \theta \\ R \cos \theta \\ p_R \sin \theta + p_\theta \cos \theta / R \\ p_R \cos \theta - p_\theta \sin \theta / R \end{pmatrix}, \quad (11)$$

where the Poisson brackets $\{x, p_x\} = 1 = \{z, p_z\}$ are preserved to obtain $\{R, p_R\} = 1 = \{\theta, p_\theta\}$. We apply the transformation (11) to (7) to obtain $H \rightarrow \mathfrak{h}$. We may once again obtain equations of motion from Hamilton's equations in the new coordinates, *i.e.* $\dot{R} = \partial_{p_R} \mathfrak{h}$, $\dot{\theta} = \partial_{p_\theta} \mathfrak{h}$. We find that

$$\dot{R}|_{R=1, \eta=1} = 0, \quad (12)$$

and that $\dot{\theta}$ does not depend on p_R , meaning that the phase-space can be reduced further to two dimensions, by restricting ourselves to pure states ($R = 1$), which stay pure with perfect measurement efficiency ($\eta = 1$), in the xz -plane; states are then parameterized entirely by the polar angle θ . No experimental detection scheme can presently achieve $\eta = 1$, but this idealized case is still useful to gain insight into the behaviors we see in more realistic forms of the system, while keeping the mathematics as simple as possible.

The stochastic Hamiltonian for the two-dimensional phase space is $h = \mathfrak{h}|_{R=1, \eta=1}$, or

$$h = p(-\Omega + r\sqrt{\gamma}(1 - \cos \theta) - \gamma \sin \theta) - \sqrt{\gamma}r \sin \theta - \frac{r^2 + \gamma(1 - \cos \theta)}{2} \quad (13)$$

where $p_\theta \rightarrow p$. The optimal readout for the MLPs is $r^* = -\sqrt{\gamma}(p(\cos \theta - 1) + \sin \theta)$, and is obtained by solving $\partial_r h|_{r=r^*} = 0$ for r^* .

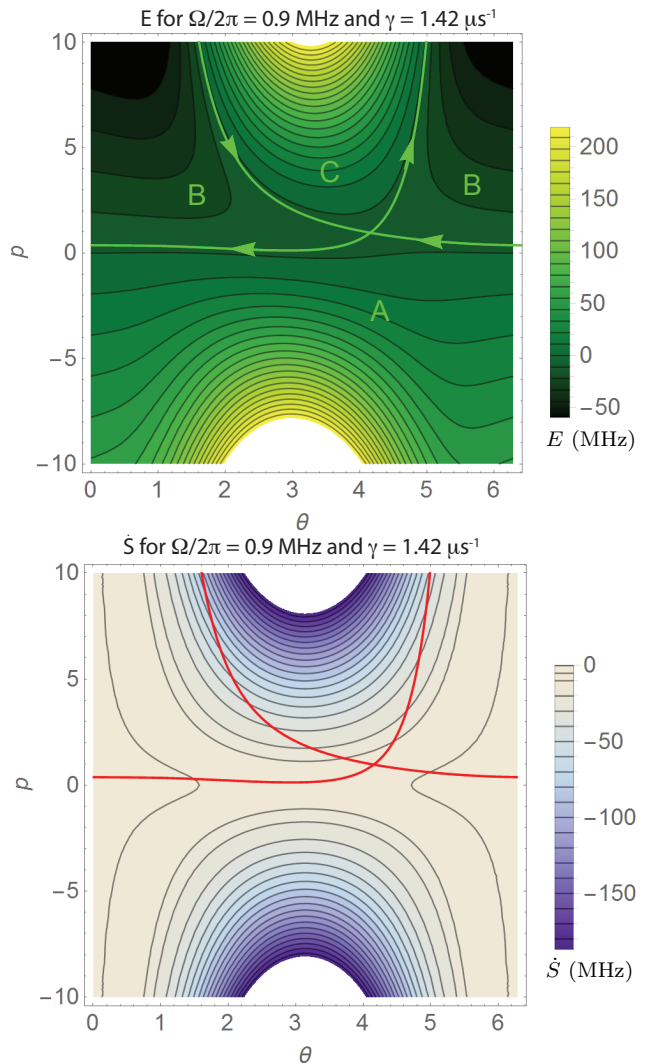


Figure 7: We show lines of constant stochastic energy (top), and lines of constant \dot{S} (bottom). E and \dot{S} are in the same units of MHz as Ω and γ . Green (top) and red (bottom) lines are those for the energy $E_c = -2.13$ MHz containing the lone fixed point at $(\theta = 4.16, \bar{p} = 0.967)$. Paths in region A all travel right to left (with the Rabi drive), and remain relatively probable over long periods of time provided they have a modest momentum/stochastic energy. Paths in region B contain both branches p_+ and p_- (16), which move in opposite directions; these paths may also have reasonably high relative probabilities to occur for initial conditions just to the left of the fixed point, over modest time evolutions (approximately less than the time required to almost a period/approach the next fixed point), but asymptote into regions of very negative \dot{S} over long time intervals. Paths in region C only go left to right (against the Rabi drive), and inhabit regions of more negative \dot{S} , meaning that they are relatively improbable over any appreciable time interval.

We additionally write the stochastic Hamiltonian with the optimal readout substituted in, which reads $h^* = a(\theta)p^2 + b(\theta)p + c(\theta)$, where we have

$$a(\theta) = \gamma \left(-\cos\theta + \frac{1 + \cos^2\theta}{2} \right), \quad (14a)$$

$$b(\theta) = -\Omega + \frac{\gamma}{2} (-3\sin\theta + \sin(2\theta)), \quad \text{and} \quad (14b)$$

$$c(\theta) = -\frac{\gamma}{2} (\cos^2\theta - \cos\theta). \quad (14c)$$

The ‘‘probability cost-function,’’ discussed in related work [16] is

$$\dot{S} = \gamma \sin^2 \left(\frac{\theta}{2} \right) (p^2 (\cos\theta - 1) + \cos\theta), \quad (15)$$

which is the integrand of the stochastic action \mathcal{S} , and describes approximately how the probability density for a MLP is affected by time spent in different regions of phase space. (The full joint probability may be written $\mathcal{P} \sim e^{\mathcal{S}}$ in the small noise approximation.) Note that $h^* = p\dot{\theta} + \dot{S}$, and therefore $\dot{S} = -ap^2 + c$. We plot the phase-portrait and contour plot of \dot{S} in Fig. 7. The phase-portrait contains lines of constant stochastic energy $E = h^*$, which may be solved to obtain functions $p_{\pm}(\theta, E)$. These have the form

$$p_{\pm}(\theta, E) = -\frac{b}{2a} \pm \sqrt{\frac{E - c}{a} + \frac{b^2}{4a^2}}, \quad (16)$$

where a , b , and c are shown in (14). Plots of the lines of constant stochastic energy (phase-portrait) and lines of constant \dot{S} are included in Fig. 7.

Hamilton’s equations are a subset of dynamical systems of the form $\dot{\mathbf{x}} = \mathbf{F}[\mathbf{x}]$, where here $\mathbf{x} = (\theta, p)$. Fixed points of a dynamical system are points $\bar{\mathbf{x}}$ which satisfy $\mathbf{F}[\bar{\mathbf{x}}] = 0$, *i.e.* denote points where the system sits still. We search for the fixed points $(\bar{\theta}, \bar{p})$ of this system, noting that

$$\dot{\theta} = 2ap + b, \quad (17a)$$

$$\dot{p} = -a'p^2 - b'p - c', \quad (17b)$$

where a , b , and c are functions defined in (14), and a' , b' , and c' are their derivatives with respect to θ . Then $\dot{\theta} = 0$ leads to $\bar{p} = -b/2a$, which may be put into the expression for $\dot{p} = 0$ to obtain

$$a' \left(\frac{b}{2a} \right)^2 - b' \left(\frac{b}{2a} \right) + c' = 0. \quad (18)$$

Any fixed-point coordinate $\bar{\theta}$ must satisfy (18). The LHS of (18) depends only on θ and the dimensionless ratio $\omega \equiv \Omega/\gamma$. We find that (18) admits one solution for $\omega > 0.145$, and three solutions for $\omega < 0.145$, shown diagrammatically in Fig. 8. We define a critical $\omega_c = 0.145$ where this bifurcation occurs. We may interpret this in terms of the optimal readout; we require

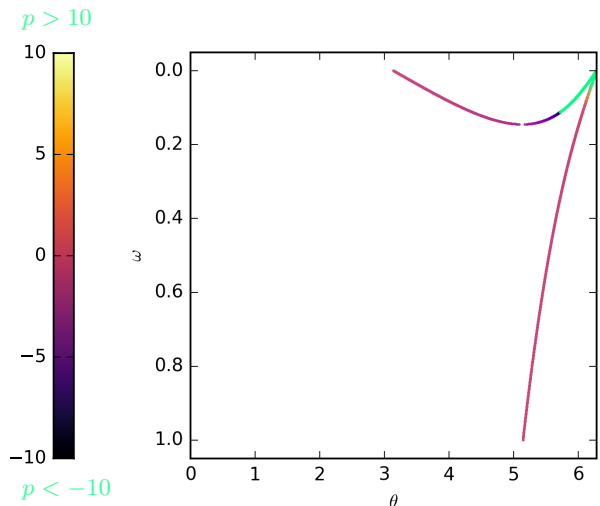


Figure 8: We plot the locations of fixed points $\bar{\theta}$ against the dimensionless parameter $\omega = \Omega/\gamma$. Color denotes momentum \bar{p} . Experimentally we operate at $\omega = 0.63 \cdot 2\pi$, where there is only one fixed point. This fixed point is a location in the phase space where the Rabi drive and fluorescence cancel. Another pair forms for $\omega < 0.145 = \omega_c$, splitting around $\theta = 5.18$. As the drive is eliminated entirely, these show system is able to stall at either the ground ($\theta = 0$ or 2π) or excited ($\theta = \pi$) states. All fixed points exist on the half of the Bloch sphere where the fluorescence and drive compete (the drive pushes the state from ground to excited, whereas the fluorescence pushes the state from excited to ground); none exist on the half where the fluorescence and drive work together (both push towards the ground state), indicating that no optimal readout can fight both the drive and spontaneous emission at the same time to hold the system still at some particular state.

that $\dot{\theta} = -\Omega - \gamma \sin\theta + r\sqrt{\gamma}(1 - \cos\theta)$ be zero, which is equivalent to a requirement that the terms for driving, fluorescence, and measurement back-action (written in that order), cancel out. The constraint on p in the MLP phase space enters indirectly through the optimal readout. We may understand a fixed point as a combined value of θ and readout where the system will sit still.

The parameters used in the accompanying experiment are $\Omega/2\pi = 0.9$ MHz and $\gamma = 1.42$ (μs) $^{-1}$, well above the value of ω where there are three fixed points. At these parameters there is only one fixed point, which sits on the separatrix of energy $E_c = -2.126$ MHz shown in Fig. 7. Its location is $(\bar{\theta}, \bar{p}) = (4.155, 0.967)$.

VII. APPENDIX: WINDING NUMBER MMLP SIMILAR TO EXPERIMENT

In Figs. 4 and 5 of the main text, we show an example of a winding number path from the four-dimensional phase space which moves from $(x_i, z_i) = (0, -0.97)$ to $(x_f, z_f) = (-0.62, 0.21)$. By simply taking the angles in-

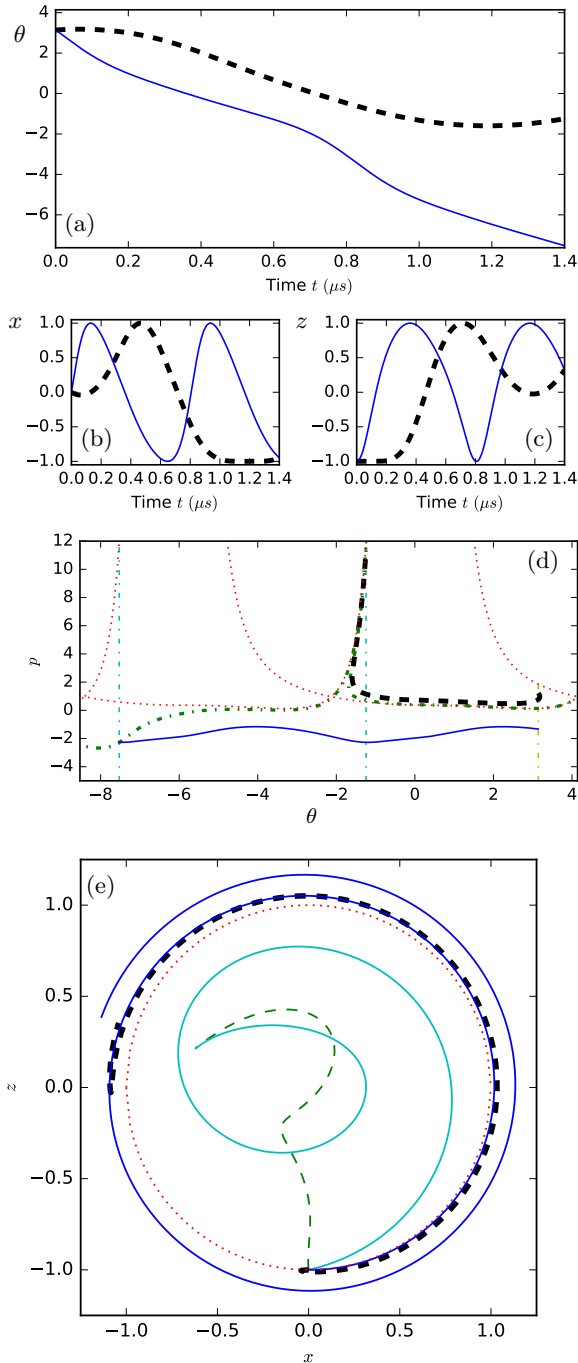


Figure 9: We show MMLPs with different winding numbers, from $\theta_i = \pi$ to either $\theta_f^{(B)} = -1.24$ (dashed black) or $\theta_f^{(A)} = -1.24 - 2\pi$ (solid blue). These are shown as $\theta(t)$ (a), $x(t)$ and $z(t)$ (b,c), and in phase space (d). In the phase space plot we show θ_i in dash-dotted yellow (the Lagrangian manifold at $t = 0$), the two θ_f in dash-dotted cyan, the separatrix in dotted red, and the Lagrangian manifold at $T = 1.4 \mu\text{s}$ in dash-dotted green. Finally, in (e) we show the pure state paths (still blue and dashed black) in the xz -plane of the Bloch sphere. The dotted red line marks the edge of the sphere; the pure-state curves are given an artificial radius outside the sphere for added visibility. The cyan and dashed green curves in (e) are the theory calculations for the example with $\eta = 0.45$ from Figs. 4 and 5 of the main text, shown for comparison.

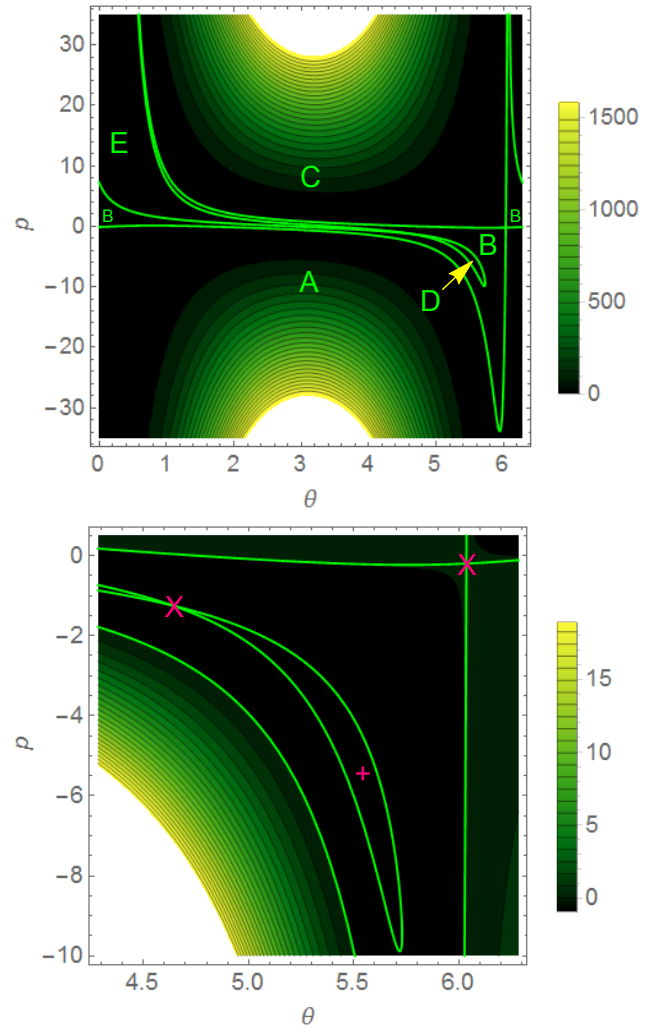


Figure 10: We include the phase portrait for $\omega = 0.13$ and $\gamma = 1$ (in the regime with three fixed points), with a complete picture (top) and reduced range to zoom in on the features of greatest interest (bottom). Two of the fixed points are hyperbolic (pink \times), at $(\bar{\theta} = 6.04, \bar{p} = -0.201)$ and $(\bar{\theta} = 4.63, \bar{p} = -1.25)$, and one is elliptical (pink $+$), at $(\bar{\theta} = 5.55, \bar{p} = -5.63)$. The latter two points are responsible for partitioning off the new regions D and E inside region B. Periodic paths are possible within the island D, which is bounded by a separatrix of energy $E_s = -0.938$ MHz. We note that for smaller ω compared with Fig. 7, we have a larger region B which now encroaches asymmetrically into A (making winding-number MMLPs less likely), and the region C has grown (indicating that it is easier for trajectories to travel against the weaker Rabi drive).

Involved, we can find a pure-state analog of this MMLP, with $\theta_i = \pi$ and $\theta_f^{(B)} = -1.24$ or $\theta_f^{(A)} = \theta_f^{(B)} - 2\pi$ (such that the number of winding counts also match the case shown from the experimental data). Mapping the mixed-state coordinates to the surface of the Bloch sphere gives us $(x_i, z_i) = (0, -1)$ and $(x_f, z_f) = (-0.95, 0.32)$. The pure-state analog reinforces the winding-number interpretation of the paths in the larger space.

In the pure state case, the faster of the two paths lives in region A of the phase space (as labeled in Fig. 7). The slower of the two paths must live in region B, because all paths in region A between the single (but periodically-repeating) fixed point actually move through that region too fast (all are past the desired point $\theta_f^{(B)}$ by the time $T = 1.4 \mu s$). We find the energy in region A which traverses the distance $\theta_i \rightarrow \theta_f^{(A)}$ in $T = 1.4 \mu s$ to be $E_A = 11.09$ MHz. We find that $E_B = -4.09$ MHz meets the boundary conditions for $\theta_f^{(B)}$.

We make an additional observation that for initial states immediately to the left of the system's fixed point, as in the case above, we see a narrow caustic in the Lagrange manifold across region B. These paths will diverge into regions of very negative \dot{S} within the caustic, meaning that the window of opportunity to actually observe MMLPs here will be somewhat short-lived, in addition to being restricted to a narrow range of initial and final states.

VIII. APPENDIX: CAUSTICS FOR SLOW DRIVE

Suppose we take $\omega = 0.13$, such that we have three fixed points in our MLP phase space instead of just one. The phase-portrait for this case is shown in Fig. 10. As $\omega \rightarrow \omega_c$ from above, region B from Fig. 7 deforms towards the shape shown in Fig. 10. When ω passes below ω_c , we see the creation of the two new fixed points which form an additional separatrix, bounding off regions D (a periodic island) and E, as labeled in Fig. 10, inside region B. The creation of an elliptic fixed point and surrounding island D of periodic MLPs is of particular interest with regards to MMLPs, because it forces the possibility of true caustics (bounded by a diverging Van-Vleck determinant), with relatively long-lived MMLPs with an onset time that could be predicted by the theory. This is true provided that the periods inside the island D are not uniform (*i.e.* vary through the island as a function of energy). This will necessarily be the case, as paths near the edge will have to slow down near the fixed point in the separatrix. Then catastrophes will be forced to appear in the Lagrangian manifold as in the example in [16]. This island will form different shapes in the manifold from the one we have studied previously, however, because it only has a fixed point in one end, rather than two, and is asymmetrically shaped. Catastrophes should also be possible to a much great extent in region B, where it is possible to choose initial states such that the manifold wraps around the island.

IX. APPENDIX: EXPERIMENTAL SETUP

The transmon circuit ($E_J/h = 24.6$ GHz, $E_C/h = 270$ MHz) was fabricated using double angle evaporation of

aluminum on a high resistivity silicon substrate. The circuit was placed at the center of a 3D aluminum waveguide cavity (dimensions $34.15 \times 27.9 \times 5.25$ mm³) which was machined from 6061 aluminum.

The cavity geometry was chosen to be resonant with the lowest energy transition of the transmon circuit. The resonant interaction between the circuit and the cavity (characterized by coupling rate $g/2\pi = 136$ MHz) results in hybrid states, as described by the Jaynes-Cummings Hamiltonian. The lowest energy transition of hybrid states ($\omega_q/2\pi = 6.3$ GHz) can therefore be considered a "one-dimensional" artificial atom because the radiative decay of the system is dominated by the cavity's coupling to a 50Ω transmission line. This radiative decay was characterized by the rate $\gamma = 1.42 \mu s^{-1}$. Resonance fluorescence from the "artificial atom" is amplified by a near-quantum-limited Josephson parametric amplifier, consisting of a 1.5 pF capacitor, shunted by a Superconducting Quantum Interference Device (SQUID) composed of two $I_0 = 1 \mu A$ Josephson junctions. The amplifier is operated with negligible flux threading the SQUID loop and produces 20 dB of gain with an instantaneous 3-dB-bandwidth of 20 MHz. The quantum efficiency was measured to be 45% [30]. We drive the qubit by sending a resonant coherent signal via a weakly coupled transmission line characterized by a Rabi frequency of $\Omega/2\pi = 0.9$ MHz.

The initial state fidelity was limited by a 3% thermal population of the excited state. The readout fidelity was enhanced by transferring the excited state population to a higher excited state of the system before applying the readout pulse [30]. All tomography results were corrected for the readout fidelity of 80%.

X. APPENDIX: STATISTICAL INFORMATION

In the main text, the finite number of post-selected trajectories contributes a statistical uncertainty in the experimental MLP. We present this as a uncertainty band indicating the standard deviation of the averaged 39 paths (Fig. 2), 18 paths (Fig. 4c), and 13 paths (Fig. 4d). Although the predicted experimental curves are in nice agreement with predicted theory curves, there are slight deviations which we attribute to limited ensemble of trajectories and finite size of post selection windows. In Fig. 6 the error bars indicate the uncertainty in the fit to the relative distribution (Eq. 10). For this fit, the values for σ_1 and σ_2 are determined from the distributions $H_1(\mathcal{E})$ and $H_2(\mathcal{E})$ and the fit determines the mean value of $P_1(0)/P_2(0)$. The error bars of Fig. 6 indicate the standard error of this mean based on the number of bins of \mathcal{E} . The number of bins is (16, 36, 22, 26) respectively left to right in Fig. 6b).

- [1] Michael V Berry and Colin Upstill. Iv catastrophe optics: morphologies of caustics and their diffraction patterns. *Progress in optics*, 18:257–346, 1980.
- [2] Vladimir Arnold. *Singularities of caustics and wave fronts*, volume 62. Springer Science & Business Media, 2013.
- [3] Tim Poston and Ian Stewart. *Catastrophe theory and its applications*. Courier Corporation, 2014.
- [4] BS White. The stochastic caustic. *SIAM Journal on Applied Mathematics*, 44(1):127–149, 1984.
- [5] H. Wiseman and G. Milburn. *Quantum Measurement and Control*. Cambridge University Press, 2010.
- [6] M. Hatridge, S. Shankar, M. Mirrahimi, F. Schackert, K. Geerlings, T. Brecht, K. M. Sliwa, B. Abdo, L. Frunzio, S. M. Girvin, R. J. Schoelkopf, and M. H. Devoret. Quantum back-action of an individual variable-strength measurement. *Science*, 339(6116):178–181, 2013.
- [7] K. W. Murch, S. J. Weber, C. Macklin, and I. Siddiqi. Observing single quantum trajectories of a superconducting qubit. *Nature*, 502:211, 2013.
- [8] A. Chantasri, J. Dressel, and A. N. Jordan. Action principle for continuous quantum measurement. *Phys. Rev. A*, 88:042110, Oct 2013.
- [9] S. J. Weber, A. Chantasri, J. Dressel, A. N. Jordan, K. W. Murch, and I. Siddiqi. Mapping the optimal route between two quantum states. *Nature*, 511:570–573, 2014.
- [10] Areeya Chantasri and Andrew N. Jordan. Stochastic path-integral formalism for continuous quantum measurement. *Phys. Rev. A*, 92:032125, Sep 2015.
- [11] Andrew N Jordan, Areeya Chantasri, Pierre Rouchon, and Benjamin Huard. Anatomy of fluorescence: quantum trajectory statistics from continuously measuring spontaneous emission. *Quantum Studies: Mathematics and Foundations*, pages 1–27, 2015.
- [12] Areeya Chantasri, Mollie E Kimchi-Schwartz, Nicolas Roch, Irfan Siddiqi, and Andrew N Jordan. Quantum trajectories and their statistics for remotely entangled quantum bits. *Physical Review X*, 6(4):041052, 2016.
- [13] F Langouche, D Roekaerts, and E Tirapegui. On the most probable path for diffusion processes. *Journal of Physics A: Mathematical and General*, 11(12):L263, 1978.
- [14] M. I. Dykman, Eugenia Mori, John Ross, and P. M. Hunt. Large fluctuations and optimal paths in chemical kinetics. *J. Chem. Phys.*, 100:5735, 1994.
- [15] A. Kamenev. *Field theory of non-equilibrium systems*. Cambridge University Press, 2011.
- [16] Philippe Lewalle, Areeya Chantasri, and Andrew N. Jordan. Prediction and characterization of multiple extremal paths in continuously monitored qubits. *Phys. Rev. A*, 95:042126, Apr 2017.
- [17] Jörg Reichardt and Stefan Bornholdt. Statistical mechanics of community detection. *Phys. Rev. E*, 74:016110, Jul 2006.
- [18] M. E. J. Newman. Finding community structure in networks using the eigenvectors of matrices. *Phys. Rev. E*, 74:036104, Sep 2006.
- [19] Santo Fortunato. Community detection in graphs. *Physics Reports*, 486:75–174, 2010.
- [20] F. Schuda, C. R. Stroud, Jr., and M. Hercher. Observation of the resonant stark effect at optical frequencies. *J. Phys. B*, 7:L198–L202, 1974.
- [21] H. J. Kimble, M. Dagenais, and L. Mandel. Photon antibunching in resonance fluorescence. *Phys. Rev. Lett.*, 39:691–695, Sep 1977.
- [22] D. F. Walls and P. Zoller. Reduced quantum fluctuations in resonance fluorescence. *Phys. Rev. Lett.*, 47:709–711, Sep 1981.
- [23] J. T. Höffges, H. W. Baldauf, W. Lange, and H. Walther. Heterodyne measurement of the resonance fluorescence of a single ion. *J. Mod. Opt.*, 44:1999–2010, 1997.
- [24] P. Kochan, H. J. Carmichael, P. R. Morrow, and M. G. Raizen. Mutual coherence and interference in resonance fluorescence. *Phys. Rev. Lett.*, 75:45–48, Jul 1995.
- [25] P. Campagne-Ibarcq, L. Bretheau, E. Flurin, A. Auffèves, F. Mallet, and B. Huard. Observing interferences between past and future quantum states in resonance fluorescence. *Phys. Rev. Lett.*, 112:180402, May 2014.
- [26] Carsten H. H. Schulte, Jack Hansom, Alex E. Jones, Clemens Matthiesen, Claire Le Gall, and Mete Atatüre. Quadrature squeezed photons from a two-level system. *nature*, 525:222–225, 2015.
- [27] D. M. Toyli, A. W. Eddins, S. Boutin, S. Puri, D. Hover, V. Bolkhovskiy, W. D. Oliver, A. Blais, and I. Siddiqi. Resonance fluorescence from an artificial atom in squeezed vacuum. *Phys. Rev. X*, 6:031004, Jul 2016.
- [28] Jens Koch, Terri M. Yu, Jay Gambetta, A. A. Houck, D. I. Schuster, J. Majer, Alexandre Blais, M. H. Devoret, S. M. Girvin, and R. J. Schoelkopf. Charge-insensitive qubit design derived from the cooper pair box. *Phys. Rev. A*, 76:042319, Oct 2007.
- [29] Hanhee Paik, D. I. Schuster, Lev S. Bishop, G. Kirchmair, G. Catelani, A. P. Sears, B. R. Johnson, M. J. Reagor, L. Frunzio, L. I. Glazman, S. M. Girvin, M. H. Devoret, and R. J. Schoelkopf. Observation of high coherence in josephson junction qubits measured in a three-dimensional circuit qed architecture. *Phys. Rev. Lett.*, 107:240501, Dec 2011.
- [30] Mahdi Naghiloo, N Foroozani, Dian Tan, A Jadbabaie, and KW Murch. Mapping quantum state dynamics in spontaneous emission. *Nature communications*, 7, 2016.
- [31] Søren Gammelmark, Brian Julsgaard, and Klaus Mølmer. Past quantum states of a monitored system. *Phys. Rev. Lett.*, 111:160401, Oct 2013.
- [32] N Foroozani, M Naghiloo, D Tan, K Mølmer, and KW Murch. Correlations of the time dependent signal and the state of a continuously monitored quantum system. *Physical review letters*, 116(11):110401, 2016.
- [33] Qing Xu and Klaus Mølmer. Intensity and amplitude correlations in the fluorescence from atoms with interacting rydberg states. *Physical Review A*, 92(3):033830, 2015.
- [34] Andrew N. Jordan and Markus Büttiker. Continuous quantum measurement with independent detector cross correlations. *Phys. Rev. Lett.*, 95:220401, Nov 2005.
- [35] Robert G. Littlejohn. The van vleck formula, maslov theory, and phase space geometry. *Journal of Statistical Physics*, 68(1):7–50, 1992.
- [36] Mark I. Dykman, Mark M. Millonas, and Vadim N. Smelyanskiy. Observable and hidden singular features of large fluctuations in nonequilibrium systems. *Physics Letters A*, 195(1):53 – 58, 1994.

- [37] P. Campagne-Ibarcq, P. Six, L. Bretheau, A. Sarlette, M. Mirrahimi, P. Rouchon, and B. Huard. Observing quantum state diffusion by heterodyne detection of fluorescence. *Phys. Rev. X*, 6:011002, Jan 2016.
- [38] D. Tan, N. Foroozani, M. Naghiloo, A. H. Kïilerich, K. Mølmer, and K. W. Murch. Homodyne monitoring of postselected decay. *Phys. Rev. A*, 96:022104, Aug 2017.